Hydrol. Earth Syst. Sci. Discuss., https://doi.org/10.5194/hess-2017-493
Manuscript under review for journal Hydrol. Earth Syst. Sci.
Discussion started: 5 September 2017

Hydrology and Earth System Sciences
Open Access
Discussions

Effects of Micro-Arrangement of Solid Particles on PCE Migration and Its Remediation in Porous Media

Ming Wu[1,2], Jianfeng Wu [1*], Jichun Wu[1**], and Bill X. Hu[2]

[1]Key Laboratory of Surficial Geochemistry, Ministry of Education; Department of Hydrosciences, School of Earth Sciences and Engineering, Nanjing University, Nanjing 210023, China

[2]Institute of Groundwater and Earth Sciences, Jinan University, Guangzhou 510632, China

Correspondence to: J.F. Wu (jfwu@nju.edu.cn), J. C. Wu (jcwu@nju.edu.cn)

Hydrol. Earth Syst. Sci. Discuss., https://doi.org/10.5194/hess-2017-493
Manuscript under review for journal Hydrol. Earth Syst. Sci.
Discussion started: 5 September 2017

Hydrology and Earth System Sciences
Open Access
Discussions

ABSTRACT

Groundwater can be stored abundantly in granula-composed aquifers with high permeability. The micro-structure of granular materials has important effect on aquifer permeability; and the contaminant migration and remediation in aquifers is also influenced by the characteristics of porous media. In this study, two different microscale arrangements of sand particles are examined to reveal the effects of micro-structure on the contaminant migration and remediation. With the help of fractal theory, the mathematical expressions of permeability and entry pressure are conducted to delineate granular materials with regular triangle arrangement (RTA) and square pitch arrangement (SPA) at microscale. Using Sequential Gaussian Simulation (SGS) method, a synthetic heterogeneous site contaminated by Perchloroethylene (PCE) is then used to investigate the migration and remediation affected by the two different micro-scale arrangements. PCE is released from an underground storage tank into the aquifer and the surfactant is used to clean up the subsurface environment. Results suggest that RTA not only can cause larger range of groundwater contamination, but also can cause harder remediation for contaminated aquifer. The PCE remediation efficiency of 60.01% -99.78% with a mean of 92.52% and 65.53% -99.74% with a mean of 95.83% are achieved for 200 individual heterogeneous realizations based on the RTA and SPA, respectively, indicating that the cleanup of PCE in aquifer with SPA is significantly easier. This study leads to a new understanding of the microstructures of porous media and demonstrates how micro-scale arrangements control contaminant migration in aquifers, which is

helpful to design successful remediation scheme for underground storage tank spill.

Keywords: microscale arrangement; regular triangle; square pitch; contaminant migration and remediation; cumulative PCE removal; macroscopic scale

1. Introduction

Groundwater is an essential natural resource for water supply to domestic, agricultural, industrial activities and ecosystem health (Boswinkel, 2000; Valipour, 2012; Valipour, 2015; Yannopoulos et al., 2015; Valipour and Singh, 2016). Unfortunately, with the rapid development of economic activities such as mining, agriculture, landfills and industrial activities (Bakshevskaia and Pozdniakov, 2016; Cui et al., 2016; Liu et al., 2016), more and more contaminants released from human activities are contaminating the precious groundwater resource and subsurface environment (Dawson and Roberts, 1997; Liu, 2005; Hadley and Newell, 2014; C.Carroll et al., 2015; Essaid et al., 2015; Huang et al., 2015; Liu et al., 2016; Schaefer et al., 2016; Weathers et al., 2016). Out of the contaminants detected in groundwater, dense nonaqueous phase liquids (DNAPLs) such as perchloroethylene (PCE) and other polycyclic aromatic hydrocarbons (PAHs), are highly toxic and carcinogenic (Dawson and Roberts, 1997; Hadley and Newell, 2014). When DNAPLs are released into aquifer from underground storage tank, they will infiltrate through the entire aquifer and form residual ganglia and pools of DNAPLs due to their large densities, high interfacial tension, and low solubility. The residual ganglia and pools of DNAPLs can serve as long-term sources of groundwater contamination that is harmful to subsurface environment and human beings (Bob et al., 2008; Liang and Lai, 2008; Liang and Hsieh, 2015). Consequently, it is very important to explore DNAPL migration in aquifer and mitigate groundwater contamination by appropriate remediation.

When DNAPL migrates in aquifers at macroscopic scale, the transport properties such as permeability, diffusivity and dispersivity are closely related to the aquifer's microstructures (Yu and Li, 2004; Yu, 2005; Yun et al., 2005; Feng and Yu, 2007; Yu et al., 2009). Therefore, characterizing the effect of microstructures on macroscopic properties is a key point of heterogeneity of porous media. In the classical Kozeny–Carman equation, the permeability K is related to porosity n, surface area S and the Kozeny constant c , where c is affected by the porosity, solid particles and micro geometric structures (Bear 1972; Yu et al. 2009). According to fractal theory, natural porous media can be treated as fractal objects (Pfeifer and Avnir 1983; Katz and Thompson 1985; Krohn 1988). For example, the tortuosity of flow path in porous media is deeply studied by various proposed fractal models (Yu and Cheng 2002; Yu et al. 2009; Cai et al. 2010), indicating the effectiveness of fractal methods compared to experimental observations. Based on fractal concepts, mathematic models are proposed to depict the permeability and invasion of fluids in some special porous media (Yu and Cheng 2002; Yu et al. 2009; Cai et al. 2010). Furthermore, fractal method is also used to explore the effect of microstructure of biological media on associated thermal conductivity while this kind of material has a complex randomly distributed vascular trees structure at microscale (Li and Yu 2013).

In this study, we focus on the effect of micro-arrangement of sand particles on macroscopic DNAPL migration and associated remediation for underground storage tank spill. With the help of fractal theory, the microstructures of two different microscale arrangements of sand particles are explored. Afterwards, the mathematical relationships between porosity and permeability, entry pressure are derived for regular triangle arrangement (RTA) and square pitch microscale arrangement (SPA). Idealized heterogeneous contaminated site is generated using Sequential Gaussian Simulation (SGS) method. Underground storage tank releases PCE into heterogeneous aquifer composed of granular material and migrates freely. After long time migration, PCE contamination is alleviated using surfactant remediation method. A multicomponent, multiphase model simulator UTCHEM is then used to simulate the entire process of DNAPL migration and remediation. Effects of arrangements of sand particles on migration and remediation of DNAPLs are comparatively analyzed based on the simulations to reveal how the microstructure of porous media controls the contaminant migration and remediation at macroscopic scale.

2. Methodology

2.1 Fractal models of two different microscale arrangements of sand particles

The porous media can be treated as the bundle of tortuous capillary tubes, the relationship between the diameter and the length of capillary tube are (Yu and Cheng, 2002):

$$L_t(\lambda) = \lambda^{1-D_t} L_s^{D_t} \tag{1}$$

where L_s is the straight length between the tortuous flow path's end point; λ is the diameter of capillary tube; D_t is the fractal dimension of tortuosity for porous media, $1<D_t<2$ (Yu and Cheng, 2002).

Select an infinitesimal element consisting of a bundle of tortuous capillary tubes form porous media, the total number of capillary tubes in infinitesimal element can be calculated by the power-law relation:

$$N(L \geq \lambda) = (\frac{\lambda_{\max}}{\lambda})^{D_f} \tag{2}$$

where D_f is the fractal dimension for pore areas in porous media, $1<D_f<2$ (Yu and Cheng, 2002); λ_{max} is the maximum diameter of capillary tubes.

Afterward, the derivative of Equation (2) can be achieved:

$$-dN(L \geq \lambda) = D_f \lambda_{\max}^{D_f} \lambda^{-(D_f+1)} d_\lambda \tag{3}$$

The total number of capillary tubes in infinitesimal element can be derived from Equation (3):

$$N_t(L \geq \lambda_{\min}) = (\frac{\lambda_{\max}}{\lambda_{\min}})^{D_f} \tag{4}$$

where λ_{min} is the minimum diameter of capillary tubes.

Dividing Equation (3) by Equation (4) can achieve:

$$-\frac{d_{N(L\geq\lambda)}}{N_t} = D_f \lambda_{\min}^{D_f} \lambda^{-(D_f+1)} d_\lambda = f(\lambda) d_\lambda \tag{5}$$

where $f(\lambda)$ is the probability density function, $f(\lambda) = D_f \lambda_{\min}^{D_f} \lambda^{-(D_f+1)}$, it should satisfy $\int_{-\infty}^{+\infty} f(\lambda) d_\lambda = 1 - (\frac{\lambda_{\min}}{\lambda_{\max}})^{D_f}$ .If $(\frac{\lambda_{\min}}{\lambda_{\max}})^{D_f} = 0$.

The probability density function satisfies the relationship:

Hydrol. Earth Syst. Sci. Discuss., https://doi.org/10.5194/hess-2017-493
Manuscript under review for journal Hydrol. Earth Syst. Sci.
Discussion started: 5 September 2017

Hydrology and Earth System Sciences
Open Access
Discussions

$$\int_{-\infty}^{+\infty} f(\lambda) d_{\lambda} = 1 - \left(\frac{\lambda_{\min}}{\lambda_{\max}}\right)^{D_f} \tag{6}$$

Considering $\left(\frac{\lambda_{min}}{\lambda_{max}}\right)^{D_f} = 0$, the above Equation (6) becomes:

$$\int_{-\infty}^{+\infty} f(\lambda) d_{\lambda} = \int_{\lambda_{\min}}^{\lambda_{\max}} f(\lambda) d_{\lambda} = 1 - \left(\frac{\lambda_{\min}}{\lambda_{\max}}\right)^{D_f} = 1 \tag{7}$$

When fluid flow in capillary tubes, the flow rate Q can be calculated by the Hagen–Poiseulle equation:

$$Q = \frac{\pi r^4 \Delta P}{8 \mu L_s} = \frac{\pi \left(\frac{\lambda}{2}\right)^4 \Delta P}{8 \mu L_s} = \frac{\pi \lambda^4 \Delta P}{128 \mu L_s} \tag{8}$$

where μ is fluid's viscosity; ΔP is the pressure gradient across the capillary tube.

The differentiation of flow rate of capillary tubes is (Yu and Cheng, 2002):

$$\begin{aligned} d_q &= [-d_{N(L \geq \lambda)}] \frac{\pi \lambda^4 \Delta P}{128 \mu L_t(\lambda)} = D_f \lambda_{\max}^{D_f} \lambda^{-(D_f+1)} d_{\lambda} \cdot \frac{\pi \lambda^4 \Delta P}{128 \mu L_t(\lambda)} \\ &= \frac{\pi}{128} \frac{\Delta P}{\mu} \frac{D_f \lambda_{\max}^{D_f}}{L_t(\lambda)} \lambda^{3-D_f} d_{\lambda} = \frac{\pi}{128} \frac{\Delta P}{\mu} \frac{D_f \lambda_{\max}^{D_f}}{\lambda^{1-D_t} L_s^{D_t}} \lambda^{3-D_f} d_{\lambda} \\ &= \frac{\pi}{128} \frac{\Delta P}{\mu} \frac{D_f \lambda_{\max}^{D_f}}{L_s^{D_t}} \lambda^{2+D_t-D_f} d_{\lambda} \end{aligned} \tag{9}$$

Integrating the individual flow rate from λ_{min} to λ_{max} can achieve the total flow rate (Yu and Cheng, 2002):

$$\begin{aligned} Q &= \int d_q = \int_{\lambda_{\min}}^{\lambda_{\max}} \frac{\pi}{128} \frac{\Delta P}{\mu} \frac{D_f \lambda_{\max}^{D_f}}{L_s^{D_t}} \lambda^{2+D_t-D_f} d_{\lambda} \\ &= \frac{\pi}{128} \frac{\Delta P}{\mu} \frac{D_f}{3 - D_f + D_t} \frac{1}{L_s^{D_T}} \lambda_{\max}^{D_f} (\lambda_{\max}^{3-D_f+D_t} - \lambda_{\min}^{3-D_f+D_t}) \\ &= \frac{\pi}{128} \frac{\Delta P}{\mu} \frac{D_f}{3 - D_f + D_T} \frac{1}{L_s^{D_t}} \lambda_{\max}^{3+D_t} \left[1 - \left(\frac{\lambda_{\min}}{\lambda_{\max}}\right)^{D_f} \left(\frac{\lambda_{\min}}{\lambda_{\max}}\right)^{3+D_t-2D_f}\right] \end{aligned} \tag{10}$$

Due to $1<D_t<2$ and $1<D_f<2$, then $3+D_T-2D_f>0$. Simultaneously, $\left(\frac{\lambda_{\min}}{\lambda_{\max}}\right)^{D_f} \cong 0$,

Hydrol. Earth Syst. Sci. Discuss., https://doi.org/10.5194/hess-2017-493
Manuscript under review for journal Hydrol. Earth Syst. Sci.
Discussion started: 5 September 2017

Hydrology and Earth System Sciences
Open Access
Discussions

$0<(\frac{\lambda_{\min}}{\lambda_{\max}})^{3+D_T-D_f}<1$. Therefore, Equation (10) can be simplified as:

$$Q=\int d_q=\frac{\pi}{128}\frac{\Delta P}{\mu}\frac{D_f}{3-D_f+D_T}\frac{1}{L_0^{D_T}}\lambda_{\max}^{3+D_T} \tag{11}$$

Substituting Darcy's law $Q=\frac{kA\Delta P}{\mu L_0}$ in Equation (11) will obtain the permeability of porous media:

$$k=\frac{\pi}{128}\frac{D_f}{3+D_T-D_f}\frac{L_0^{1-D_T}}{A}\lambda_{\max}^{3+D_T} \tag{12}$$

To obtain the fractal dimension of tortuosity D_t, the expression of tortuosity (τ) can be obtained from Equation (1):

$$\tau=\frac{L_t(\lambda)}{L_s}=\frac{\lambda^{1-D_t}L_s^{D_t}}{L_s}=(\frac{L_s}{\lambda})^{D_t-1} \tag{13}$$

Then the D_f is given by (Yu and Li, 2001):

$$D_t=1+\frac{\ln\tau}{\ln(\frac{L_s}{\lambda})} \tag{14}$$

RTA and SPA are shown in Fig. 1. An equilateral triangle and a square are selected from the two micro-structures as unit cells (Fig. 1a and Fig. 1b). The unit cell of equilateral triangle is composed of three solid particles and the pore among them, while the unit cell of square is composed of four solid particles. For the unit cell of RTA in Fig. 1a, corresponding porosity is given by:

$$n=\frac{A_a-\pi R_v^2/2}{A_a} \tag{15}$$

where n is porosity; A_a is the total area of equilateral triangle; R_v is the average radius of solid particles. The total area of equilateral triangle can be achieved:

$$A_a=\frac{\pi R_v^2}{2(1-n)} \tag{16}$$

Hydrol. Earth Syst. Sci. Discuss., https://doi.org/10.5194/hess-2017-493
Manuscript under review for journal Hydrol. Earth Syst. Sci.
Discussion started: 5 September 2017

Hydrology and Earth System Sciences
Open Access
Discussions

The side length of the equilateral triangle in Fig. 1a can be calculated as:

$$L_a = R_v \sqrt{\frac{2\pi}{\sqrt{3}(1-n)}} \tag{17}$$

where L_a is the side length.

The area of irregular pore among solid particles is given by:

$$A_{ap} = A_a - \frac{\pi R_v^2}{2} = \frac{\pi R_v^2 n}{2(1-n)} \tag{18}$$

where A_{ap} is the area of pore in the unit cell.

Approximate the pore in the equilateral triangle as a circle, then the maximum diameter of pore can be obtained:

$$\lambda_{max,a} = R_v \sqrt{\frac{2n}{1-n}} \tag{19}$$

where $\lambda_{max,a}$ is the diameter of capillary tube in equilateral triangle. The fluid passes not only the central-pore of the unit cell, but also the gap between adjacent particles. The gap length and the average diameter of capillary tube perpendicular to the plane of equilateral triangle are calculated as follows:

$$\Delta L_a = L_a - 2R_v = R_v\left(\sqrt{\frac{2\pi}{\sqrt{3}(1-n)}} - 2\right) \tag{20}$$

$$\lambda_a = \frac{\lambda_{\max,a} + \Delta L_a}{2} = \frac{R_v}{2}\left(\sqrt{\frac{2n}{1-n}} + \sqrt{\frac{2\pi}{\sqrt{3}(1-n)}} - 2\right) \tag{21}$$

where ΔL_a is the gap length between solid particles; λ_a is the average diameter of capillary tubes in the equilateral triangle.

Generally, the tortuosity of flow path in porous media is the ratio of the length of tortuous flow path to the straight length of flow path along the flow direction (Taiwo et al., 2016):

$$\tau = \frac{L_t}{L_s} \tag{22}$$

where L_t is the length of tortuous flow path; and L_s is the straight length of flow path along the flow direction.

For the flow path shown in Fig. 1a, the L_t and L_s respectively are:

$$L_t = (h_o - R_v) + \frac{\pi R_v}{2} = R_v(\sqrt{\frac{\sqrt{3}\pi}{2(1-n)}} + \frac{\pi}{2} - 1) \tag{23}$$

$$L_s = h_o = R_v\sqrt{\frac{\sqrt{3}\pi}{2(1-n)}} \tag{24}$$

where h_o is the altitude of the equilateral triangle, $h_o = \frac{\sqrt{3}}{2}L_a = R_v\sqrt{\frac{\sqrt{3}\pi}{2(1-n)}}$.

Consequently, the tortuosity of RTA is yielded:

$$\tau = \frac{L_t}{L_s} = 1 + \frac{\frac{\pi}{2} - 1}{\sqrt{\frac{\sqrt{3}\pi}{2(1-n)}}} \tag{25}$$

The D_f is determined using Sierpinkski gasket (Fig. 2) in fractal theory (Yu and Cheng, 2002). The shaded area represents solid of porous media and the white area represents pore. The pore area fractal dimension in Figs. 2a-c are 0.000, 1.000 and 1.594, respectively ($1 = L_a^{D_f} = 2^{D_f}$, $3 = L_a^{D_f} = 3^{D_f}$, $13 = L_a^{D_f} = 5^{D_f}$). Based on the Sierpinkski gasket, the dimensionless pore area in RTA (Fig. 1a) is approximated as:

$$A_{apd} = (L_a^+)^{D_f} \tag{26}$$

where A_{apd} is the dimensionless pore area of RTA; $L_a^+ = L_a / \lambda_{min}$. Equation (26) can be solved to achieve D_f:

$$D_f = \frac{\ln A_{apd}}{\ln L_a^+} \tag{27}$$

Hydrol. Earth Syst. Sci. Discuss., https://doi.org/10.5194/hess-2017-493
Manuscript under review for journal Hydrol. Earth Syst. Sci.
Discussion started: 5 September 2017

Hydrology and Earth System Sciences
Open Access
Discussions

The porosity equals to the ratio of the dimensionless pore area of RTA (A_{apd}) to the dimensionless total area of RTA (A_a^+):

$$n = \frac{A_{apd}}{A_a^+} \tag{28}$$

where $A_a^+ = \frac{A_a}{\pi\lambda_{\min}^2/4} = \frac{\frac{\pi R_v^2}{2(1-n)}}{\pi\frac{\lambda_{\min}^2}{4}} = \frac{2R_v^2}{\lambda_{\min}^2}\frac{1}{1-n} = \frac{(d^+)^2}{2}\frac{1}{1-n}$; $d^+ = \frac{2R_v}{\lambda_{\min}}$., $L_a^+ = \sqrt{A_a^+}$.

From Equation (28), the dimensionless pore area of RTA (A_{apd}) is given by:

$$A_{apd} = n \cdot A_a^+ \tag{29}$$

The dimensionless total area of RTA (A_a^+) can be written as:

$$A_a^+ = (L_a^+)^2 \tag{30}$$

Afterward, L_a^+ is calculated as:

$$L_a^+ = \sqrt{A_a^+} = \sqrt{\frac{(d^+)^2}{2}\frac{1}{1-n}} = d^+\sqrt{\frac{1}{2(1-n)}} \tag{31}$$

Substituting Equation (29) and Equation (31) into Equation (27) will derive D_f of RTA:

$$D_f = \frac{\ln A_{apd}}{\ln L_a^+} = \frac{\ln(n \cdot A_a^+)}{\ln(\sqrt{A_a^+})} = 2 + \frac{\ln(n)}{\ln(\sqrt{A_a^+})} = 2 + \frac{\ln(n)}{\ln(d^+\sqrt{\frac{1}{2(1-n)}})} \tag{32}$$

For the unit cell of square shown in Fig. 1b, the porosity is:

$$n = \frac{A_b - \pi R_v^2}{A_b} \tag{33}$$

where A_b is the total area of the square. Equation (33) can also be expressed as the area of unit cell:

$$A_b = \frac{\pi R_v^2}{1-n} \tag{34}$$

Hydrol. Earth Syst. Sci. Discuss., https://doi.org/10.5194/hess-2017-493
Manuscript under review for journal Hydrol. Earth Syst. Sci.
Discussion started: 5 September 2017

Again, the side length of the square is:

$$L_b = \sqrt{A_b} = R_v\sqrt{\frac{\pi}{1-n}} \tag{35}$$

Consequently, the area of irregular pore in the square is given by:

$$A_{bp} = A_b - \pi R_v^2 = \frac{n\pi R_v^2}{1-n} \tag{36}$$

where A_{bp} is the area of pore in the square.

Approximate the pore as a circle and obtain corresponding maximum diameter:

$$\lambda_{max,b} = 2R_v\sqrt{\frac{n}{1-n}} \tag{37}$$

where $\lambda_{max,b}$ is the maximum diameter of capillary tube perpendicular to the plane of the square. Similarly, fluid flows through the central-pore in the square and the gap between adjacent particles. As a result, the gap and average diameter of capillary tube are expressed as:

$$\Delta L_b = L_b - 2R_v = R_v\left(\sqrt{\frac{\pi}{1-n}} - 2\right) \tag{38}$$

$$\lambda_b = \frac{\lambda_{max,b} + \Delta L_b}{2} = \frac{R_v}{2}\left(2\sqrt{\frac{n}{1-n}} + \sqrt{\frac{\pi}{1-n}} - 2\right) \tag{39}$$

where ΔL_b is the gap length between the adjacent two solid particles; λ_b is the average diameter of capillary tube.

For the tortuous flow path in Fig. 1b, the L_t and L_s respectively are given by:

$$L_t = \Delta L_b + \pi R_v = R_v\left(\sqrt{\frac{\pi}{1-n}} - 2 + \pi\right) \tag{40}$$

$$L_s = L_b = R_v\sqrt{\frac{\pi}{1-n}} \tag{41}$$

Afterward, the tortuosity of SPA yields:

$$\tau = \frac{L_t}{L_s} = 1 + \frac{\pi - 2}{\sqrt{\frac{\pi}{1 - n}}} \tag{42}$$

The procedure of deriving D_f of SPA is similar to the procedure of calculating D_f of RTA. Similarly, the D_f and porosity of SPA (Fig. 1b) are given by:

$$D_f = \frac{\ln A_{bpd}}{\ln L_b^+} \tag{43}$$

$$n = \frac{A_{bpd}}{A_b^+} \tag{44}$$

where A_{bpd} is the dimensionless pore area of SPA; $L_b^+ = L_b / \lambda_{min}$, A_b^+ is the dimensionless total area of SPA, $A_b^+ = \frac{A_b}{\pi\lambda_{\min}^2/4} = \frac{\frac{\pi R_v^2}{1-n}}{\pi\frac{\lambda_{\min}^2}{4}} = \frac{4R_v^2}{\lambda_{\min}^2}\frac{1}{1-n} = (d^+)^2\frac{1}{1-n}$.

The dimensionless pore area of SPA (A_{bpd}) can be yielded from Equation (44):

$$A_{bpd} = n \cdot A_b^+ \tag{45}$$

L_b^+ can be calculated as:

$$L_b^+ = \sqrt{A_b^+} = \sqrt{(d^+)^2\frac{1}{1-n}} = d^+\sqrt{\frac{1}{1-n}} \tag{46}$$

Substituting Equation (45) and Equation (46) into Equation (43), D_f of SPA can be derived:

$$D_f = \frac{\ln A_{bpd}}{\ln L_b^+} = \frac{\ln(n \cdot A_b^+)}{\ln(\sqrt{A_b^+})} = 2 + \frac{\ln(n)}{\ln(\sqrt{A_b^+})} = 2 + \frac{\ln(n)}{\ln(d^+\sqrt{\frac{1}{1-n}})} \tag{47}$$

The entry pressure of tortuous capillary tube (P_c) is defined by Yong-Laplace equation as follows (Ahn and Seferis, 1991):

$$P_c = \frac{\omega}{\lambda}\frac{1-n}{n} \tag{48}$$

where P_c is the entry pressure; λ is the diameter of capillary tube; ω equals to $F\sigma\cos\theta$

in which θ is the contact angle between fluid and solid, σ is the surface tension of the wetting fluid, and F is the form factor depending on the capillary tube alignment and the flow direction.

2.2 Dealing with the heterogeneity of porous media

In this study, Sequential Gaussian Simulation (SGS) is used to generate random realization of heterogeneous porosity field. SGS is a stochastic simulation method combining sequential principle and Gaussian method. It assumes variable fit to Gaussian random field. The gauss distribution function is constructed at the each simulated spatial location based on the characteristics of variation function, afterward, randomly selects a value as the variable at the location. In SGS method, observation data are transformed to Gaussian distribution or normal distribution. Based on current sample data, the conditional probability distribution of points to be simulated is calculated by SGS method and then simulation is performed based on semivariogram model. Each simulated value, together with measured data and previous simulation data, becomes the conditional data set for the next step. As simulation proceeds, the conditional data set increases. Pervious researches suggested 50–400 realizations are required to obtain a statistically stable mean realization (Eggleston et al., 1996; Hu et al., 2007).

2.3 Modeling PCE migration and its remediation

The DNAPL migration and remediation are modeled using a multi-component, multi-phase, and multi-composition of contaminant-transport processes simulator named

UTCHEM (University of Texas Chemical Compositional Simulator) (Delshad et al., 1996). As an extension to Delshad's work, UTCHEM was developed by University of Texas as a comprehensive and practical tool. In numerous applications, UTCHEM has proved to be particularly useful and has been a popular multi-phase flow and multi-constituent, reactive transport model used widely in groundwater simulations. UTCHEM account for chemical, physical and biological reactions, complex non-equilibrium sorption, decay and geochemical reactions and surfactant-enhanced solubilization and mobilization of DNAPLs, moreover, heterogeneous properties of porous media is addressed. As a result, UTCHEM has been adapted for a variety of environmental applications such as surfactant-enhanced aquifer remediation (SEAR). In this study, DNAPL migration and remediation for cleaning up DNAPL contamination in idealized heterogeneous site are simulated by UTCHEM.

3. Application to a synthetic heterogeneous PCE contaminated site

3.1 Site description

The idealized domain synthetic application is a two-dimensional confined aquifer saturated by water (Fig. 3). The length, width and depth of aquifer are 101 m, 25 m and 25 m, respectively. Idealized aquifer is discretized into 101 grids horizontally and 25 layers vertically (Fig. 3b). The spacing of each grid is uniformly 1 m along x and z directions, and the longitudinal and transverse dispersivities are set as to 1.0 m and 0.1 m, respectively. Horizontal and vertical correlation length values is 5 m. The top and bottom borders of aquifer are defined as no-flow boundaries, while the left and right borders are defined as constant potential boundaries to create a groundwater flow from left to right under a low hydraulic gradient of 0.005 m/m (Liu et al., 2003; Liu, 2005; Qin et al., 2007). The porous media of idealized aquifer is assumed to be heterogeneous and mixed by different grades of sands.

The porosity of aquifer is assumed spatially and uniformly distributed with average value of 0.220 and standard deviation of 0.060. In this study, porosity follows normal distribution and its standard deviation (SD) represents the enhanced geological heterogeneity. 200 realizations porosity field are generated using Sequential Gaussian Simulation (SGS). One of the 200 realizations of heterogeneous field is shown in Fig. 4a. Simultaneously, statistical assessment is taken on the individual realization of porosity field and corresponding histograms are shown in Fig. 4b. We can find the frequency of the individual realization of porosity field is close to normal distribution, which conform to the fact that most characteristic of natural aquifer can be expressed as normal distribution (Montgomery et al, 1987). Based on the heterogeneous porosity field, the fractal dimension of tortuosity D_t, the fractal dimension for pore areas D_f and the diameter of capillary tube in porous media, permeability is obtained by the Equation (12). Fig. 4c shows the individual heterogeneous permeability field selected from the 200 realizations of RTA, besides, the result of associated frequency analysis is shown in Fig. 4d. The permeability field fits the lognormal distribution obviously, which has been presented by many researches that the parameter of aquifer penetrability is lognormal distribution field (Montgomery et al., 1987; Veneziano and Tabaei, 2004). Compared to histogram of porosity field in Fig. 4b, the shape of permeability is similar. The individual heterogeneous permeability field of SPA is shown in Fig. 4e. Corresponding frequency analysis of SPA reveals the permeability field is lognormal distribution, while some difference appears compared with RTA (Fig. 4f). The average permeability of individual realization of RTA is 2.012×10^{-12} m^2 and the average permeability of individual realization of SPA is 1.618×10^{-12} m^2. For 200 realizations, the average permeability of RTA and SPA are 2.120×10^{-12} m^2 and 1.706×10^{-12} m^2, indicating the permeability of RTA is bigger than SPA slightly.

The average pore diameters of two different microscale arrangements of particles are derived using corresponding fractal models. In detail, average diameter of RTA is calculated by Equation (21) and average diameter of SPA is calculated by Equation (39). Consequently, the entry pressure of the two kinds of microscale arrangements can be obtained by Equation (48), respectively. The individual entry pressure fields of two microscale arrangements and associated frequency analysis are shown in Figs. 4g-j. From the frequency of entry pressure in Fig. 4h and Fig. 4j, the entry pressures of both RTA and SPA are the lognormal distributions. However, the average entry pressure of individual realization of RTA is 1.980 kPa, while the average entry pressure of SPA is 1.481 kPa. For 200 realizations of entry pressure field, the average entry pressure of RTA is 1.922 kPa and the average entry pressure of SPA is 1.442 kPa. The differences of average entry pressure and the entry pressure distributed range between RTA and SPA imply the micro-structure of aquifer has effect on the macroscopic characteristics.

The purpose of this study is to explore the effects of micro-structure of aquifer on DNAPL migration and remediation. A PCE spill event (the leaking of underground storage tank) occurs on the top of the aquifer and a surfactant remediation is desired to clean up the contaminated aquifer. The total duration of 300 days is divided into four stages: (1) 300 m^3 PCE is released from underground storage tank into aquifer at the top layer of spill position shown in Fig. 3a during 0~30 days; (2) PCE migrates in aquifer freely during 30~100 days; (3) surfactant is injected into aquifer during 100~150 days; and (4) water flushing during 150~300 days. In the first stage, PCE is released as a point pollution source in the center grid block at the top layer of the aquifer, which spill is at a constant rate of 10 m^3/day. After PCE coming into heterogeneous aquifer, PCE is migrating freely under the effects of gravity and the natural hydraulic gradient condition. The PCE not only migrates downward through the aquifer, but also can be trapped by capillary forces as residual ganglia and globules. During the long-term PCE migration period, PCE is contaminating groundwater and expanding plume. To clean up the contaminated aquifer, 4% surfactant solution is injected into aquifer through the two injection wells (Fig. 3b) at a constant rate of 80 m^3/day, simultaneously, contaminated groundwater is extracted through production well at constant rate of 160 m^3/day. Surfactant can reduce the interfacial tension between DNAPL and aqueous phase to promote solubilization and mobilization of DNAPL in aquifer. After surfactant injection, the contaminated aquifer is flushed by water over a long time of 150 days. Based on the distributions of porosity, permeability and entry pressure of two microscale arrangements, the entire PCE migration and remediation process is simulated by a multicomponent, multiphase model simulator UTCHEM (Delshad et al., 1996). The parameters used in simulation are listed in Table 1. Simulation results of two different microscale

Hydrology and Earth System Sciences
Discussions
Open Access

arrangements are compared to reveal the effect of microstructure on the DNAPL migration and remediation.

3.2 Results and discussion

3.2.1 PCE migration and its remediation based on single realizations

The simulation results of PCE migration for individual realization of porosity field for RTA are shown in Fig. 5a-f. When PCE is released into aquifer into aquifer at the top layer of spill position, PCE almost infiltrates vertically under the effect of gravity force (Fig. 5a). Due to the heterogeneity of aquifer, some preferential flow appears and PCE plume becomes irregular (Fig. 5b). After 30 days, PCE plume almost touches the bottom of aquifer (Fig. 5c). When the PCE leakage is stopped, PCE continues to migrate freely in aquifer for 70 days (Fig. 5d-f). The released PCE is migrating downward and entrapped by capillary forces as residual ganglia and globules. Heterogeneity of aquifer makes PCE migrate along preferential pathway. When PCE plume touches the zones of low permeability and high entry pressure, it will bypass these zones and migrate continuously, which leads to an increasing variability in PCE distribution. After PCE plume reaches the bottom of aquifer, PCE begins accumulate and form contaminant pool at the bottom. At t=100 days, A PCE pool has been formed at the bottom of aquifer, moving toward the right boundary.

Figs. 6a-f show the simulated PCE saturation for individual realization of porous media for SPA during migration period. Under the effects of gravity force and natural hydraulic gradient, PCE is migrating and spreading contaminant plume. Heterogeneity

Hydrol. Earth Syst. Sci. Discuss., https://doi.org/10.5194/hess-2017-493
Manuscript under review for journal Hydrol. Earth Syst. Sci.
Discussion started: 5 September 2017

Hydrology and Earth System Sciences
Open Access
Discussions

of aquifer significantly changes the migration paths and leads to irregular morphology of the PCE plume (Figs. 6a-c). However, due to the different micro-arrangement of aquifer, the entry pressure field also is different which leads to some differences. After the PCE injection, the simulated PCE saturation in Figs. 6d-f indicates that further trapping and spreading of the PCE occurs during this period. Compared with the simulation results of RTA in Fig. 5, the PCE plume slightly seems similar in Fig. 6. Moreover, PCE infiltrate more quickly in porous media of RTA in Fig. 5. After 70 days, PCE plume has touched the bottom for RTA (Fig. 5e), while PCE plume based on SPA still keeps a significant distance from bottom (Fig. 6e).

To clean up the DNAPL, 4% surfactant solution is injected through two injection wells at a constant rate of 80 m^3/day over 50 days to evaluate the effectiveness of surfactant flushing. Afterwards, following water-flush is applied during 150~300 day. The location of injection wells and production well are presented in Fig. 3b. The production well is rightly installed at the location of the PCE spill position and two injection wells are located 39 m to the left and right of the production well. Figs. 5g-l shows the PCE remediation results of individual realization for RTA. During the early remediation period, the effect of cleaning up DNAPL is not yet apparent (Figs. 5g-i). When the water flushing begins, the surfactant solution circulates throughout the contaminated aquifer (Figs. 5j-l). At t=200 days, there has been 237.01 m^3 PCE removal from contaminated aquifer, occupying 79.00% of the total released PCE (Fig. 5j). As time goes on, 268.30 m^3 PCE is removed from aquifer and remediation efficiency reaches 89.43%.

The same surfactant remediation is also conducted for individual realization of porous media for SPA. Compare with the remediation for RTA, the remediation effect is more apparent for SPA (Figs. 6g-l). As the remediation processes, more DNAPL is removed and less DNAPL is remained as small contaminant pools at the bottom of aquifer. At t=200 day, 267.68 m^3 PCE is removed from contaminated aquifer, corresponding remediation efficiency rise to 89.23%. At t=300 day, 285.32 m^3 PCE is cleaned up and remediation efficiency reaches 95.11%. From results of remediation, it is obvious that microstructure has effect on remediation of macroscopic scale aquifer. Results suggest contaminated aquifer of RTA is hard to clean up by surfactant remediation while SPA can improve DNAPL remediation efficiency.

3.2.2 PCE migration and SGS realizations

PCE migration and remediation processes are simulated for 200 realizations of porosity field for porous media of RTA and SPA. The variations of contaminant mass, the ganglia-to-pool ratio (GTP) and moments of PCE plume versus time are presented in Figs. 7a-h. During 0~30 day, the PCE in aquifer increases linearly at a constant rate of 10 m^3/day (Fig. 7a), which corresponding to contaminant spill stage. Afterward, PCE volume keep constant during the second stage ranged 30~100 day, while PCE in aquifer is reduced when surfactant is injected into aquifer. After surfactant and water flushing the contaminated aquifer, most DNAPL is cleaned up. The residual DNAPL mass remained in aquifer of 0.67 m^3-119.89 m^3 with a mean of 22.42 m^3 and 0.79 m^3-103.33 m^3 with a mean of 12.51 m^3 are achieve for 200 individual heterogeneous realizations based on the RTA and SPA, respectively. The average remediation efficiency of SPA is undoubtedly higher than RTA, indicating the aquifer of SPA is easier to clean up. PCE plume architectures are quantified by measuring the ganglia-to-pool ratio (GTP) in Fig. 7b. Over entire periods, curves of GTP value appear obvious oscillations. Surfactant has the ability of promoting solubilization and mobilization of DNAPL can reduce GTP value. As a result, when surfactant is injected at t=100 day, the GTP value reduces quickly. When surfactant injection is end and water flushing begins, the GTP value increases with steep flank slope. At last, GTP values reach 0.10-0.41 with a mean of 0.21 and 0.15-0.42 with a mean of 0.28 for 200 individual heterogeneous realizations based on the RTA and SPA, respectively.

Fig. 7c shows cumulative PCE removal from contaminated aquifer versus flushing time for RTA and SPA. During the surfactant injection period ranged 100~150 day, the DNAPL removal is not apparent, However, DNAPL is removed effectively and quickly during water flushing period. Through long time remediation, the removal PCE from contaminated aquifer reach 179.89 m^3-298.98 m^3 with a mean of 277.29 m^3 and 196.45 m^3-298.87 m^3 with a mean of 287.21 m^3 for 200 realizations based on RTA and SPA, respectively. Average remediation efficiency of SPA (95.83%) is obvious higher than average remediation efficiency of RTA (92.52%).

Fig. 7d shows the GTP value as a function of cumulative PCE removal for contaminated aquifer. The GTP remains at a relatively low level before 30% of the DNAPL is removed from aquifer. When 40% of the total 300 m^3 PCE are removed, GTP values are increasing and corresponding curves appear a wave crest because the high saturation zone of PCE plume are dissolved and turned into ganglia state. After the wave crest, the GTP values decline quickly with steep flank slope due to PCE ganglia removal through water flushing. At last, GTP values increase at the end of remediation process for 200 realizations, indicating most of PCE is removed and most of residual PCE turn to ganglia state.

For the center of PCE plume in horizontal axis, associated variations versus time are similar for 200 realizations based on RTA and SPA (Fig. 7e). Significantly, the PCE plume vertical infiltration rate in aquifer of RTA is slightly faster than PCE infiltration in aquifer of SPA for 200 realizations (Fig. 7f). Simultaneously, the second PCE plume moments in horizontal direction of RTA are different from SPA (Fig. 7g). After PCE migration at natural condition at 100 day, the second PCE plume moments in horizontal direction are 10.61 m^2-40.50 m^2 with a mean of 21.51 m^2 and 10.99 m^2-36.38 m^2 with a mean of 20.75 m^2 for 200 realizations based on RTA and SPA, respectively. At t=300 day, the second PCE plume moments in horizontal direction change to 0.81 m^2-34.88 m^2 with a mean of 5.79 m^2 and 1.03 m^2-24.57 m^2 with a mean of 4.64 m^2 for RTA and SPA, respectively. The horizontal second moment of RTA is always larger than horizontal second moment of SPA, indicating the PCE plume in aquifer of RTA is wider than PCE plume in aquifer of SPA and RTA can cause larger range of groundwater contamination. Similarly, the second moments in vertical direction of RTA are larger than the second moments in vertical direction of SPA.

4. Conclusions

The micro-structure of aquifer has important effect on macroscopic scale characteristics of aquifer and inner contaminant migration and remediation. In this study, we focus on the DNAPL migration and remediation in heterogeneous aquifer composed of granular porous media with RTA and SPA. The microscale models of RTA and SPA are developed to obtain the mathematical expressions of permeability and entry pressure using fractal method. 200 realizations of porosity field are generated using SGS method and PCE is released from underground storage tank into heterogeneous aquifer. To clean up contamination caused by underground storage tank spill, surfactant remediation technique is used to remove contaminants in aquifer. The entire process of DNAPL migration and remediation is simulated by a multicomponent, multiphase model simulator UTCHEM. Results suggest RTA not only cause larger range of groundwater contamination than RTA, but also the contaminated aquifer of RTA is harder to clean up compared with SPA. The second PCE plume moments in horizontal direction are 10.61 m^2-40.50 m^2 with a mean of 21.51 m^2 and 10.98 m^2-36.38 m^2 with a mean of 20.75 m^2 for 200 realizations based on RTA and SPA after PCE natural migration at t=100 day, respectively. Furthermore, the second PCE plume moments in horizontal direction at t=300 day are 0.807 m^2-34.88 m^2 with a mean of 5.79 m^2 and 1.025 m^2-24.57 m^2 with a mean of 4.64 m^2 for RTA and SPA respectively after long time remediation. Simultaneously, the residual DNAPL mass remained in aquifer are 0.67 m^3-119.89 m^3 with a mean of 22.42 m^3 and 0.79 m^3-103.33 m^3 with a mean of 12.51 m^3 for RTA and SPA respectively, indicating remediation efficiency of SPA (65.53%-99.74% with a mean of 95.83%) mostly is higher than remediation efficiency of RTA (60.01%-99.78% with a mean of 92.52%). This study proves microstructure of aquifer has important effect on contaminant movement and associated remediation efficiency in macroscopic scale aquifer, which is very essential and significant for dealing with the accidental event of underground storage tank spill and identifying subsurface contaminant source in the future.

Acknowledgments

This research was financially supported by the National Key Research and Development Plan of China (2016YFC0402807, 2016YFC0402802 and 2016YFC0402800), the National Natural Science Foundation of China-Xianjiang project (U1503282), and the National Natural Science Foundation of China (41372235).

References

Ahn, K.J., Seferis, J.C.: Simultaneous measurements of permeability and capillary pressure of thermosetting matrices in woven fabric reinforcements, Polym. Composite., 12, 146-152, 1991.

Bakshevskaia, V.A., Pozdniakov, S.P., Simulation of hydraulic heterogeneity and upscaling permeability and dispersivity in Sandy-Clay foormations, Math. Geosci., 48, 45-64, 2016.

Bear, J.: Dynamics of fluids in porous media, Dover, New York, 1972.

Bob, M.M., Brooks, M.C., Mravik, S.C., Wood, A.L.: A modified light transmission visualization method for DNAPL saturation measurements in 2-D models, Adv. Water Resour., 31, 727-742, 2008.

Boswinkel, J.A.: International Groundwater Resources Assessment Centre (IGRAC),

Hydrol. Earth Syst. Sci. Discuss., https://doi.org/10.5194/hess-2017-493
Manuscript under review for journal Hydrol. Earth Syst. Sci.
Discussion started: 5 September 2017

Netherland Institute of Applied Geoscience, Netherlands, 2000.

Cui, Q.L., Wu, H.N., Shen, S.L., Yin, Z.Y., Horpibulsuk, S.: Protection of neighbour buildings due to construction of shield tunnel in mixed ground with sand over weathered granite, Environ, Earth Sci., 75, 458, 2016.

C.Carroll, K., McDonald, K., Marble, J., Russo, A.E., Brusseau, M.L.: The impact of transitions between two-fluid and three-fluid phases on fluid configuration and fluid-fluid interfacial area in porous media, Water Resour. Res., 51, 7189-7201, 2015.

Dawson, H.E., Roberts, P.V.: Influence of Viscous, Gravitational, and Capillary Forces on DNAPL Saturation, Groundwater, 35(2), 261-269, 1997.

Delshad, M., Pope, G.A., Sepehrnoori, K.: A compositional simulator for modeling surfactant enhanced aquifer remediation, 1 Formation, J. Contam. Hydrol., 23, 303-327, 1996.

Eggleston, J.R., Rojstaczer, S.A., Peirce, J.J.: Identification of hydraulic conductivity structure in sand and gravel aquifers: Cape Cod data set, Water Resour. Res., 32, 1209–1222, 1996.

Essaid, H.I., Bekins, B.A., Cozzarelli, I.M., Organic contaminant transport and fate in the subsurface: Evolution of knowledge and understanding, Water Resour. Res., 51, 4861-4902, 2015.

Feng, Y.J., Yu, B.M.: Fractal dimension for tortuous streamtubes in porous media, Fractals, 15, 385-390, 2007.

Hadley, P.W., Newell, C.: The New Potential for Understanding Groundwater

Contaminant Transport, Groundwater, 52(2), 174-186, 2014.

Hu, K., White, R., Chen, D., Li, B., Li, W.: Stochastic simulation of water drainage at the field scale and its application to irrigation management, Agr. Water Manage., 89, 123-130, 2007.

Huang, J.Q., Christ, J.A., Goltz, M.N., Demond, A.H.: Modeling NAPL dissolution from pendular rings in idealized porous media, Water Resour. Res., 51, 8182-8197, 2015.

Katz, A.J., Thompson, A.H.: Fractal sandstone: Implications for conductivity and pore formation, Phys. Rev. Lett., 54, 325-332, 1985.

Krohn, C.E.: Sandstone fractal and Euclidean pore volume distributions, J. Geophys. Res., 93, 3286-3296, 1988.

Liang, C., Hsieh, C.L.: Evaluation of surfactant flushing for remediating EDC-tar contamination, J. Contam. Hydrol., 177-178, 158-166, 2015.

Liang, C., Lai, M.C.: Trichloroethylene degradation by zero valent iron activated persulfate oxidation, Envrion. Eng. Sci., 25(7), 1071-1077, 2008.

Liu, H., Li, Y.X., He, X., Sissou, Z., Tong, L., Yarnes, C., Huang, X.: Compound-specific carbon isotopic fractionation during transport of phthalate esters in sandy aquifer, Chemosphere, 144, 1831-1836, 2016.

Liu, L.: Modeling for surfactant-enhanced groundwater remediation processes at DNAPLs-contaminated sites, J. Environ. Inform., 5(2), 42-52, 2005.

Liu, L., Hao, R.X., Cheng, S.Y.: A possibilistic analysis approach for assessing environmental risks from drinking groundwater at petroleum-contaminated sites,

J. Environ. Inform., 2(1), 31-37, 2003.

Liu, Y., Wang, S., McDonough, C.A., Khairy, M., Muir, D.C.G., Helm, P.A., Lohmann, R.: Gaseous and freely-dissolved PCBs in the lower great lake based on passive sampling: spatial trends and air-water exchange, Environ. Sci. Technol., 50, 4932-4939, 2016.

Pfeifer, P., Avnir, D.: Chemistry in Nonintegral dimensions between two and three. I . Fractal theory of heterogeneous surface, J. Chem. Phys., 79, 3558-3565, 1983.

Qin, X.S., Huang, G.H., Chakma, A., Chen, B., Zeng, G.M.: Simulation-based process optimization for surfactant-enhanced aquifer remediation at heterogeneous DNAPL-contaminated sites, Sci. Total Environ., 381, 17-37, 2007.

Schaefer, C.E., White, E.B., Lavorgna, G.M., Annable, M.D.: Dense nonaqueous-phase liquid architecture in fractured bedrock: implications for treatment and plume longevity, Environ. Sci. Technol., 50, 207-213, 2016.

Valipour, M.: Comparison of surface irrigation simulation models: Full hydrodynamic, zero inertia, kinematic wave, J. Agr. Sci., 4(12), 68-74, 2012.

Valipour, M.: Future of agricultural water management in Africa, Arch, Agron. Soil Sci., 61(7), 907-927, 2015.

Valipour, M., Singh, V.P.: Global experiences on wastewater irrigation: challenges and Prospects, in: Maheshwari, B., Singh, V.P., Thoradeniya, B., Balanced urban development: options and strategies for liveable cities, Volume 72 of the series Water Science and Technology Library, pp. 289-327, 2016.

Veneziano, D., Tabaei, A.: Nonlinear spectral analysis of flow through porous media with isotropic lognormal hydraulic conductivity, J. Hydrol., 294, 4-17, 2004.

Weathers, T.S., Harding-Marjanovic, K., Higgins, C.P., Alvarez-Cohen, L., Sharp, J.O.: Perfluoroalkyl acids inhibit reductive dechlorination of Trichloroethene by repressing dehalococcoides, Environ. Sci. Technol., 50, 240-248, 2016.

Yannopoulos, S.I., Lyberatos, G., Theodossiou, N., Li, W., Valipour, M., Tamburrino, A., Angelakis, A.N.: Evolution of water lifting devices (pumps) over the centuries worldwide, Water, 7, 5031-5060, 2015.

Yu, B.M.: Fractal character for tortuous streamtubes in porous media, CHIN. PHYS. LETT., 22, 158-160, 2005.

Yu, B.M., Cai, J.C., Zou, M.Q.: On the physical properties of apparent two-phase fractal porous media, Vadose Zone J., 8, 177-186, 2009.

Yu, B.M., Cheng, P.: Fractal models for the effective thermal conductivity of bidispersed porous media, J. Thermophys. Heat Tr., 16, 22-29, 2002.

Yu, B.M., Li, J.H.: A geometry model for tortuosity of flow path in porous media, CHIN. PHYS. LETT., 21, 1569-1571, 2004.

Yun, M.J., Yu, B.M., Zhang, B., Huang, M.T.: A geometry model for tortuosity of streamtubes in porous media with spherical particles, CHIN. PHYS. LETT., 22(6), 1464-1467, 2005.

595 **Table 1.** Parameters used in simulation

Parameter	Value
Average value of porosity	0.22
Standard deviation of porosity	0.06
Longitudinal dispersivity	1.0 m
Transverse dispersivity	0.1 m
Hydraulic gradient	0.005 m/m
Water density	1.00 g/cm^3
PCE density	1.63 g/cm^3
Surfactant density	1.15 g/cm^3
Water viscosity	1.00 cp
PCE viscosity	0.89 cp
PCE/ Water interfacial tension	45 dyn/cm
PCE solubility in water	240 mg/L
Residual water saturation	0.24
Residual PCE saturation	0.17
Endpoint of Water (BC model)	0.486
Endpoint of PCE (BC model)	0.65
Exponent of Water (BC model)	2.85
Exponent of PCE (BC model)	2.7
Exponent of capillary pressure	-0.52

Figure Captions

Figure 1. Two different microscale arrangements of solid particles: (a) RTA; and (b) SPA

Figure 2. Three kinds of Sierpinkski gasket [30]: (a) L_a=2; (b) L_a=3; and (c) L_a=5

Figure 3. (a) Two-dimensional view of contaminated domain; and (b) locations of injection extraction wells

Figure 4. (a) The individual porosity field generated by Sequential Gaussian Simulation (SGS) method; (b) the frequency of individual porosity field; (c) the individual permeability field of RTA obtained from individual porosity field; (d) the frequency of individual permeability field for RTA; (e) the individual permeability field of SPA obtained from individual porosity field; (f) the frequency of individual permeability field for SPA; (g) The obtained individual entry pressure field of RTA; (h) the frequency of individual entry pressure field of RTA; (i) the obtained individual entry pressure field of SPA; and (j) the frequency of individual entry pressure of SPA

Figure 5. Simulated PCE saturation for individual realization of RTA over the entire migration and remediation periods (0~300 day)

Figure 6. Simulated PCE saturation for individual realization of SPA over the entire migration and remediation periods (0~300 day)

Figure 7. (a) PCE volume in aquifer versus time, RTA represents RTA and SPA represents SPA; (b) Changes in GTP as a function of time; (c) Cumulative DNAPL removal as a function of time; (d) Variation of GTP value as a function of cumulative DNAPL removal percent; (e) the change of the center of PCE

Hydrol. Earth Syst. Sci. Discuss., https://doi.org/10.5194/hess-2017-493
Manuscript under review for journal Hydrol. Earth Syst. Sci.
Discussion started: 5 September 2017

plume during the entire periods of migration and remediation; (f) the change of the depth of PCE plume center during the entire periods; (g) variation of second PCE plume moment in horizontal axis; and (h) variation of second PCE plume moment in vertical axis

Figure 1

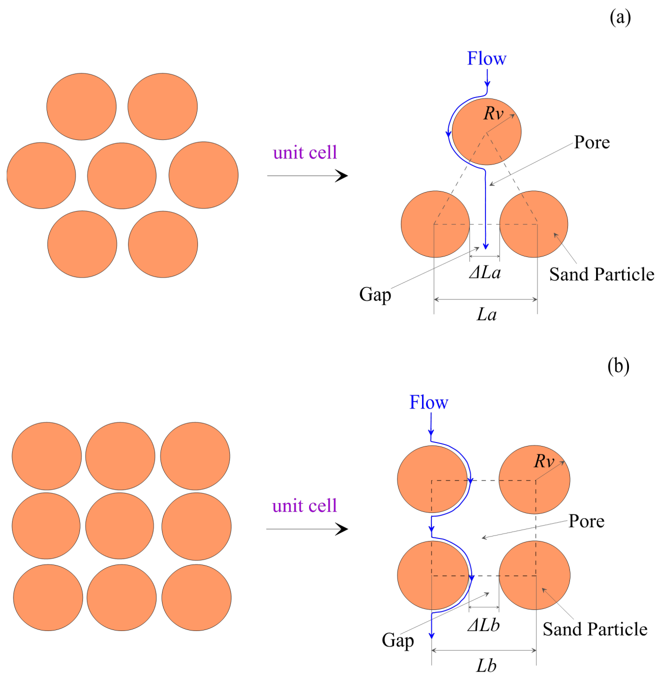
(a)
Flow
unit cell
Rv
Pore
Sand Particle
Gap
ΔLa
La
(b)
Flow
unit cell
Rv
Pore
Sand Particle
Gap
ΔLb
Lb

Hydrol. Earth Syst. Sci. Discuss., https://doi.org/10.5194/hess-2017-493
Manuscript under review for journal Hydrol. Earth Syst. Sci.
Discussion started: 5 September 2017

Figure 2

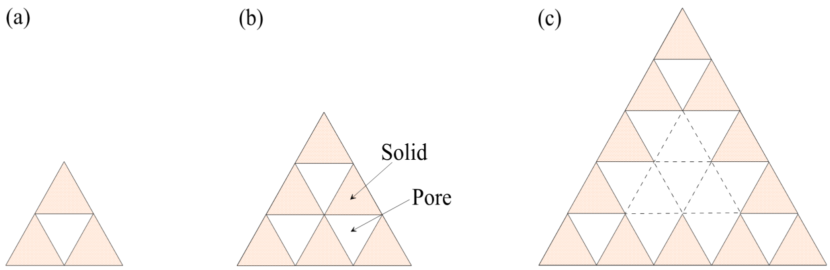

636 **Figure 3**

637

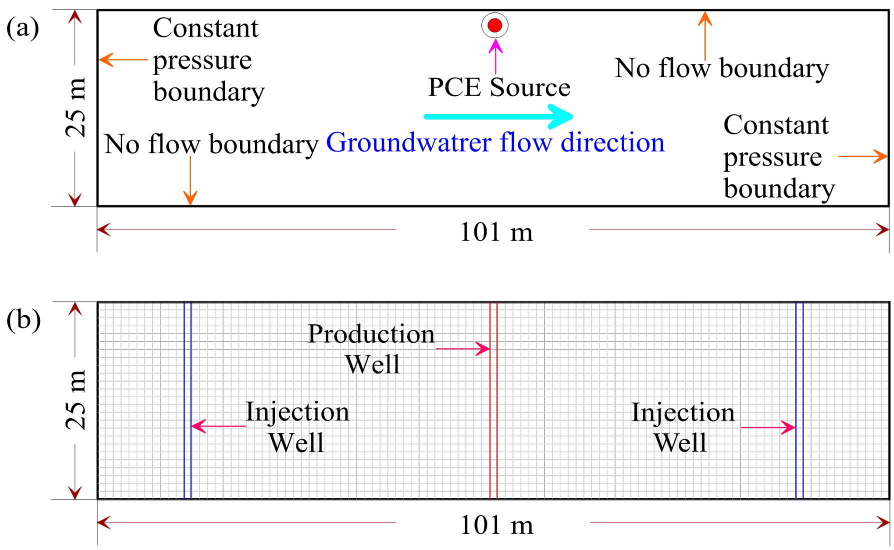

638

639

Hydrol. Earth Syst. Sci. Discuss., https://doi.org/10.5194/hess-2017-493
Manuscript under review for journal Hydrol. Earth Syst. Sci.
Discussion started: 5 September 2017

Hydrology and Earth System Sciences
Open Access
Discussions

Figure 4

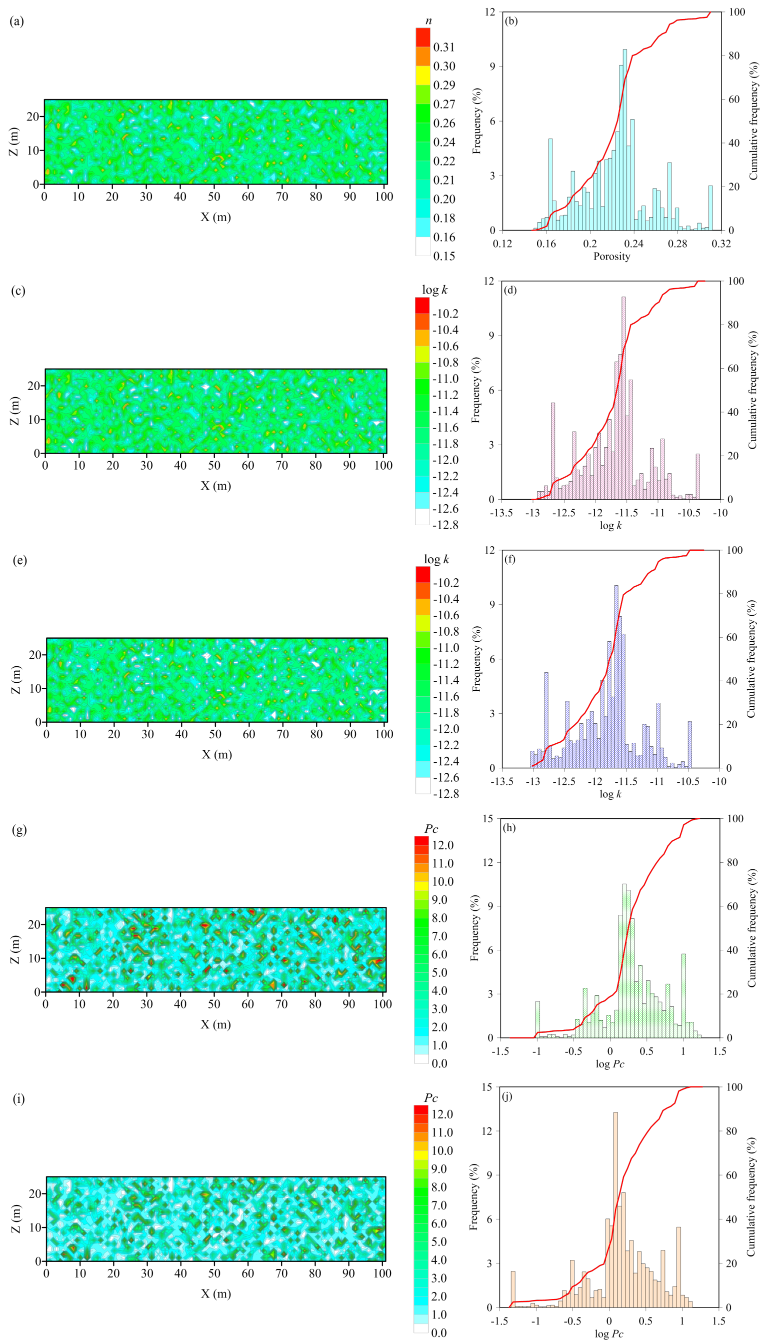

Figure 5

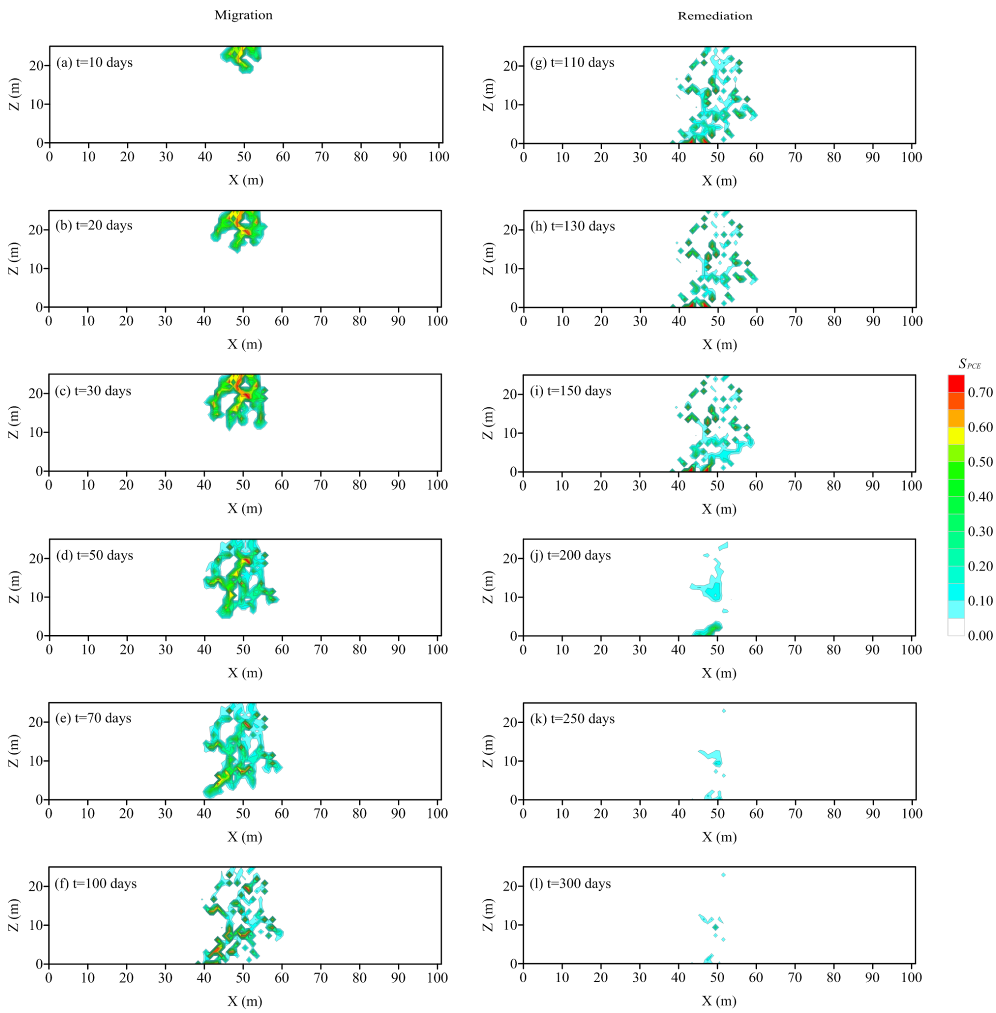
Migration
Remediation
(a) t=10 days
(b) t=20 days
(c) t=30 days
(d) t=50 days
(e) t=70 days
(f) t=100 days
(g) t=110 days
(h) t=130 days
(i) t=150 days
(j) t=200 days
(k) t=250 days
(l) t=300 days
Z (m)
X (m)
S_{PCE}
0.70
0.60
0.50
0.40
0.30
0.20
0.10
0.00

Hydrol. Earth Syst. Sci. Discuss., https://doi.org/10.5194/hess-2017-493
Manuscript under review for journal Hydrol. Earth Syst. Sci.
Discussion started: 5 September 2017

Hydrology and Earth System Sciences
Open Access
Discussions

652 **Figure 6**

653

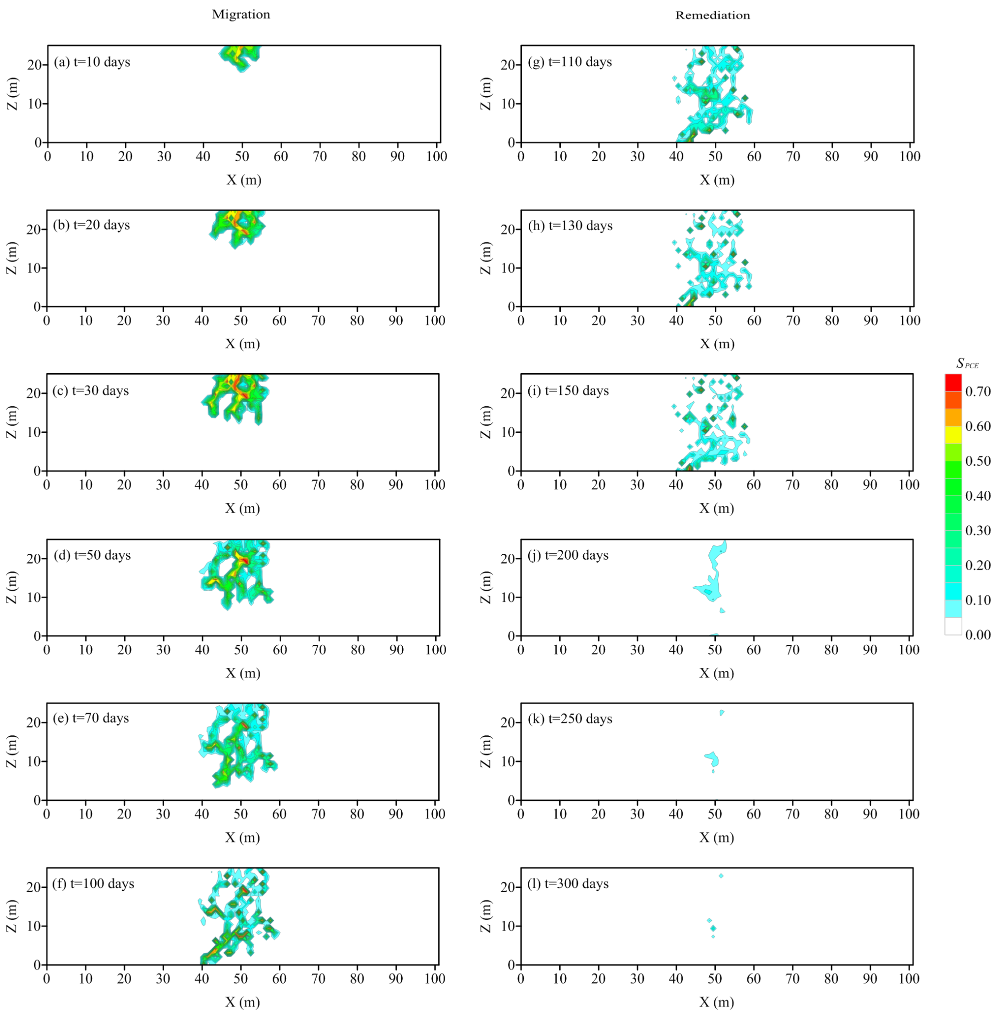

654

655

656 **Figure 7**

657

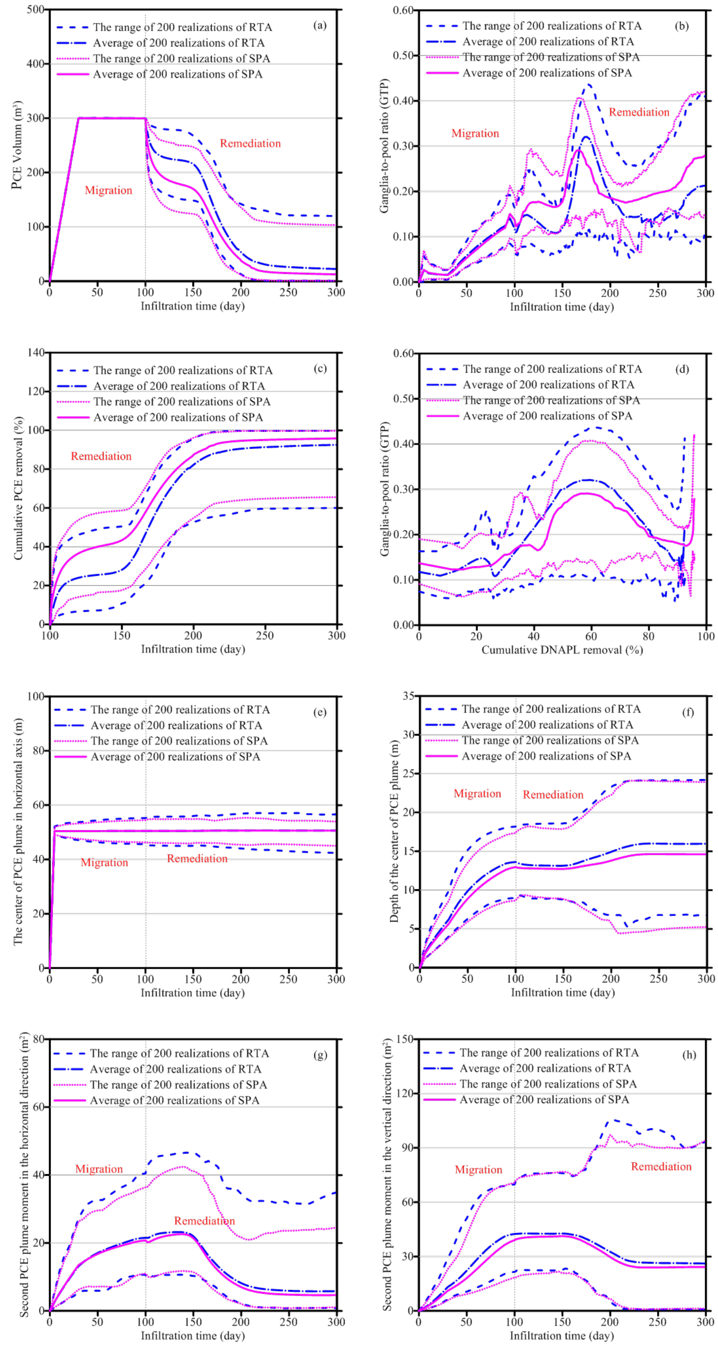

658